Bayesian optimization of origami multi-cell tubes for energy absorption considering mixed categorical-continuous variables

Na Qiu [a], Zhuoqun Yu [a], Depei Wang [a], Mingwei Xiao [a], Yiming Zhang [b,*], Nam H. Kim [c], Jianguang Fang [d,*]

[a] School of Mechanical and Electrical Engineering, Hainan University, Haikou, 570228, China
[b] The State Key Laboratory of Fluid Power and Mechatronic Systems, Zhejiang University, Hangzhou, 310027, China
[c] Department of Mechanical & Aerospace Engineering, University of Florida, Gainesville, FL 32611, USA
[d] School of Civil and Environmental Engineering, University of Technology Sydney, Sydney, NSW 2007, Australia

ABSTRACT

Multi-cell structures have been widely utilized in energy-absorbing applications for their lightweight and superior mechanical properties. However, they may produce high peak forces that are harmful to occupant safety during a vehicle collision. In addition, the naturally formed folding and global bending modes under axial loads can significantly restrict their energy-absorbing capability. In this study, a novel origami multi-cell structure is proposed to avoid excessive peak loads and at the same time to guide the deformation mode to improve the energy-absorbing capability. Four cross-sectional types of origami multi-cell structures are investigated experimentally and numerically. The results indicated that the web-to-web (W2W) type origami multi-cell structures are most promising for energy absorption, while web-to-corner (W2C) structures yield low peak forces and excellent deformation modes in our study cases. To further exploit the potential of these structures, multi-objective optimization is required to consider the conflicting objectives of maximizing energy-absorbing capability and minimizing the peak force. However, it is challenging for traditional optimization to deal with continuous, integer, and categorical variables simultaneously. Therefore, the Bayesian optimization method based on the Hamming distance is utilized to handle mixed categorical-continuous variables to optimize origami multi-cell tubes. The optimization results indicated that the optimal origami W2C can decrease the peak force by 30 % while keeping a similar level of specific energy-absorbing capability compared with the conventional W2C structure. Moreover, the optimal origami W2C structure can improve the energy absorption by 40 % compared with the origami W2C baseline design.

1. Introduction

Energy-absorbing devices dissipate kinetic energy through plastic deformation during impact events to protect the lives of occupants. Thin-walled tubes are widely utilized as energy absorbers [1–3] due to their excellent impact resistance, lightweight, and ease-of-processing performances. Furthermore, various efficient energy-absorbing structures such as foam-filled [4,5], sandwich [6,7], multi-cell structures [8–10], and Lattice structures [11–13] have been proposed to enhance the energy-absorbing capability of thin-walled tubes.

In general, the multi-cell structures place more materials at the intersections within the cross-section and exhibit excellent energy-absorbing capability compared to the conventional mono-cell

counterparts [14,15]. Najafi et al. [16] investigated the energy absorption properties of multi-cell tubes with different connections among the outer, rib plates, and inner tubes. Zhang et al. [17] revealed that the deformation mode is sensitive to the different cross-sections in nested corrugated square energy-absorbing tubes. These studies demonstrated the significant potential of multi-cell tubes in energy absorption. However, their folding patterns are naturally formed, and the tube may even collapse in a global bending mode under axial crushing, as shown in Fig. 1, which is usually inefficient for energy absorption [18]. In addition, the peak force of the multi-cell structure is also relatively high (see Fig. 1), which is not preferable and even dangerous during a vehicle collision. Therefore, how to reduce the peak load and enhance the energy-absorbing capability by controlling their deformation modes

---

* Corresponding authors.
E-mail addresses: yimingzhang@zju.edu.cn (Y. Zhang), Jianguang.Fang@uts.edu.au (J. Fang).

simultaneously has drawn a lot of attention.

To trigger the collapse mode and reduce the maximum force, corrugations [19–22], origami [23–28], and grooves [29–33] have been introduced to the surface of thin-walled structures. Among them, origami structures can lead to pre-designed deformation patterns to produce the desired mechanical response. For example, Song et al. [34] studied the energy-absorbing capability of an origami pattern tube under axial loading. They found that the origami tubes can effectively lower the initial peak force and achieve a more uniform crush load than the conventional tube. Zhou et al. [35] found that the trapezoidal origami pattern can trigger the full diamond pattern. Ma et al. [36] investigated a gradient origami tube and found that the force response of the origami tube could be tuned by the gradient of folding angle and module height. However, its overall energy-absorbing capability did not change significantly. Zhou et al. [37] studied the origami tubes under low-velocity impact load and found that the origami tubes outperform conventional square tubes in energy absorption. As depicted in Fig. 1, while the pre-designed origami patterns could guide the stable collapse mode and reduce the maximum force, they would also reduce the overall energy absorption due to the introduced weakening of the whole structure [23].

The previous studies mainly focused on origami structures [37–39] or multi-cell structures [16,40] alone. To the authors' best knowledge, the combination of origami patterns and multi-cell structures has been less studied [25]. To exploit the full potential of thin-walled tubes, a new origami multi-cell structure is proposed by combining multi-cell structures [16] and origami patterns [41].

Effective optimization algorithms play a crucial role in the exploration of design spaces, as highlighted in previous works [42,43]. While traditional structural optimization methods have primarily been employed in discrete [44–46] and continuous design spaces [47], they often fall short when dealing with categorical design variables, such as distinct configurations. This presents a formidable challenge in the optimization process. To address this issue, some approaches involve optimizing each configuration individually or selecting the most promising configuration for optimization. The ultimate optimal design solution is then determined based on either engineers' expertise [8] or employing multi-attribute decision-making (MADM) techniques [2,48, 49].

The conventional approach of optimizing multiple categories separately proves to be inefficient from the viewpoint of structural optimization. Addressing the challenge of optimizing across multiple categories necessitates expanding the design space to incorporate mixed-categorical variables. For instance, Li et al. [50] employed techniques such as K-nearest neighbor, Random forest, Support vector machine, and Artificial neural network to consider categorical variables (e.g., deformation mode) and effectively mitigate undesired deformations, thereby enhancing optimization accuracy.

In the realm of Bayesian optimization over combinatorial spaces, various strategies have been introduced. These include methods like variational autoencoders (VAEs) [51], one-hot transformation [52], and inherently discrete models (e.g., random forests [53]). However, accurately quantifying uncertainty in scenarios involving both continuous and categorical variables remains a challenge. Gaussian processes have also been applied to combinatorial space problems. Two noteworthy strategies can be summarized as follows: the utilization of a hierarchical structure, as seen in the Model-based Algorithm Configuration (SMAC) [54], and employing kernel-based approaches involving the Gower distance [55] and relaxation techniques [56]. Nevertheless, random sample points are unreliable in hierarchical approaches, and kernel-based methods are often constrained by complex interactions among distinct feature variables.

An alternative approach that can overcome the abovementioned limitations involves handling mixed data by employing combined kernels for Gaussian processes [57]. This entails utilizing a Hamming kernel within the categorical subspace [54] and a squared-exponential kernel within the continuous subspace. By combining these kernels, more complex interactions among different feature variables can be captured. In this study, a Gaussian process-based Bayesian optimization algorithm is proposed for optimizing origami multi-cell structures using combined kernels. This approach is well-suited for handling mixed categorical-continuous variables.

The rest of this paper is organized as follows. First, the geometric design of the origami multi-cell tube is given in Section 2. Numerical modeling and its validation are elaborated in Section 3. A novel Bayesian optimization method based on the Hamming distance is used to optimize the origami multi-cell structures in Section 4. The conclusions are drawn in Section 5.

2. Design of origami multi-cell structures

2.1. Geometry

The origami multi-cell structure proposed herein consists of an outer origami tube, connecting rib plates and an inner tube (as shown in Fig. 2). The outer tube is a square cross-sectional configuration tube with
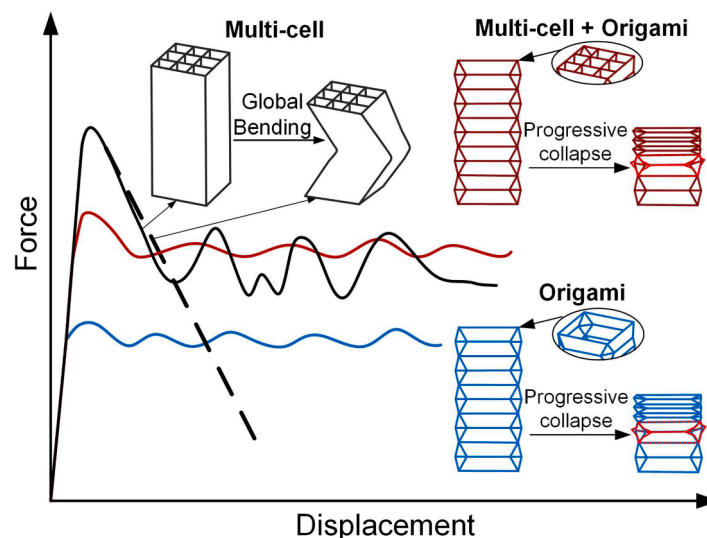

Fig. 1. Schematic diagram of force–displacement curves for multi-cell, origami, and proposed origami multi-cell structures.
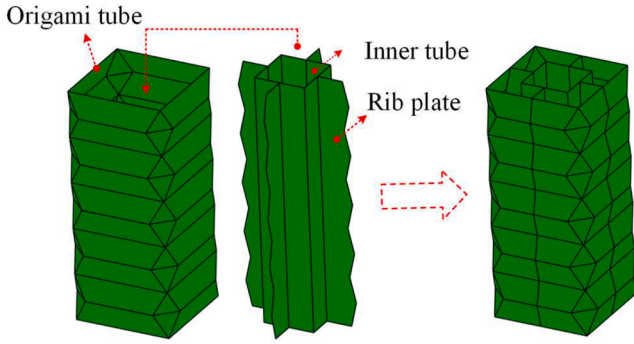
Fig. 2. Origami multi-cell structure configuration.

the diamond origami pattern, and the inner tube is a straight tube with a square cross-sectional configuration. The outer and inner tubes are connected by the ribs to form an origami multi-cell structure.

In this study, four types of origami multi-cell structures are constructed as shown in Fig. 3(a): (a) web-to-web (W2W): ribs connecting the outer and inner webs at the mid-wall; (b) W2C: ribs connecting the outer web to the inner corner; (c) C2C: ribs connecting the outer corner to the inner corner; (d) C2W: ribs connecting the outer corner to the inner web. The thicknesses of the outer origami walls, connecting ribs, and inner tubes are t_1, t_2, and t_3, respectively. The width of the outer tube is 60 mm and that of the inner tube is 30 mm, which is determined by referring to the size of real automotive energy absorbers and the previous multi-cell designs [16,58].

As depicted in Fig. 3(b–d), a diamond origami module with a certain folding angle is designed on the outer tube. This origami module plays two roles: (a) a pre-designed geometric imperfection to reduce the peak crushing force; and (b) a folding trigger to guide the origami multi-cell structure to produce a controlled deformation pattern during the compression process. Specifically, Fig. 3(b) represents the unfolding diagram of an origami module, where the solid lines represent the mountain folds and the dashed lines represent valley folds. As shown in Fig. 3(c), an origami module can be constructed by folding the planar structure shown in Fig. 3(b) along these creases and then connecting the free edges.

The relationship between the width of the origami pattern c and the unfolded height of the origami module l can be established by [59]

$$\theta = 2\arccos\left[\left(\sqrt{2}-1\right)\frac{c}{l}\right] \tag{1}$$

where θ is the folding angle. The origami module is determined by the width of the origami module b, the width of the diamond origami pattern c, and the height of the origami module l. When c equals 0, the origami pattern tube is transformed into a conventional straight tube of square cross-section with a folding angle of 180° (see Fig. 3(d)).

As shown in Fig. 3(e–g), an origami module's upper end is the same square as its lower end. Thus, the designed origami tubes are composed of multiple origami modules connecting end to end. For example, Fig. 3 (e) illustrates an origami tube with five modules, where h denotes the folded height of a single module and M denotes the module number. In this case, the folded height of the origami tube H can be calculated by Mh and the unfolded height of the origami pattern tube L can be given as Ml. The geometric relationship between L and H can be formulated by

$$H = L\sin\frac{\theta}{2} \tag{2}$$

2.2. Geometric relationship

Fig. 3(f) depicts the diamond pattern variation with different module numbers when the folding angle equals 150°. It is observed that the diamond pattern gradually shrinks as M increases. Because the ratio of the width c of the diamond pattern to the unfolded height l of the module remains constant when the folding angle is kept constant. As M increases, the unfolded height l of the diamond pattern becomes smaller and smaller. Hence, the width c of the diamond pattern also becomes smaller and smaller to keep the folding angle unchanged.

When module number M and the unfolded height l of the diamond origami pattern are kept constant, the width c of the diamond origami pattern becomes smaller and smaller as the folding angle increases. Fig. 3(g) shows the variation of the origami pattern for different folding angles when M is fixed at 3.

3. Numerical modeling

3.1. Finite element modeling

The explicit finite element solver LS-DYNA 971 was used in this paper to numerically investigate the collapse behaviors and energy-
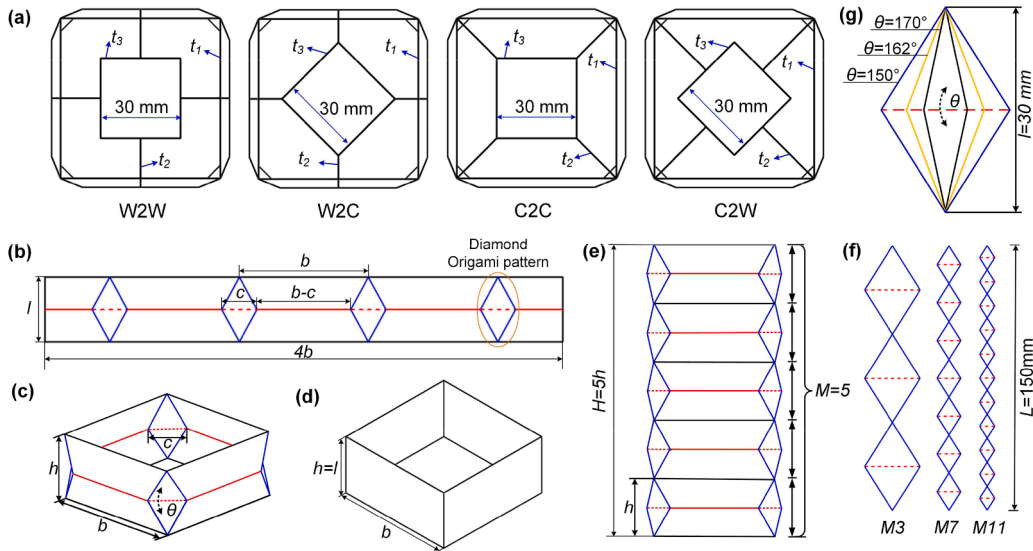

Fig. 3. (a) Four section types of origami multi-cell structures, (b) an unfolded origami module, (c) an origami module, (d) a conventional square tube, (e) origami pattern tube, (f) scheme of diamond origami pattern with different module number M when folding angle $\theta = 150°$, (g) scheme of diamond origami pattern with different folding angles θ when module number $M = 3$.

absorbing capabilities of the origami multi-cell structures under quasi-static loading. The finite element (FE) model is made up of moving and fixed rigid plates, as well as multi-cell origami structures with various cross-sectional arrangements and patterns (see Fig. 4(a)). To simulate the quasi-static loading, the top moving plate moves downwards from the top end of the tubes along the axial direction at a constant velocity of 1 m/s [60]. It was observed the ratio of the kinetic energy to the total energy remained below 5 % throughout the simulation, indicating the dynamic effect is insignificant and the velocity of 1 m/s can be considered quasi-static loading conditions. The bottom fixed, rigid plate restrains the tubes' bottom ends. The origami multi-cell structure was meshed using Belyschko–Tsay four-node shell elements with five-point integration through the thickness. The mesh size of the shell element was set to 1.5 mm according to a convergence study of the mesh size as shown in Fig. 4(b). The contacts between the origami multi-cell structures and moving/fixed rigid plates were simulated by the "AUTOMATIC_SURFACE_TO_SURFACE" contact constraint. While the self-contact inside the origami multi-cell structure was defined by the "AUTOMATIC_SINGLE_SURFACE" constraint. The friction coefficients for both types of contacts were set to 0.25 [61].

The material used for the origami multi-cell structures was 316L steel and the elastic-plastic material model MAT24 in LS-DYNA was employed. To obtain the material properties, the tensile sample made with 316L stainless steel was tested under the uniaxial tensile condition. The corresponding true stress–strain curve is shown in Fig. 4(c). The mechanical properties were Young's modulus $E = 145$ GPa, yield strength $\sigma_s = 538.593$ MPa, ultimate tensile strength $\sigma_u = 603.698$ MPa, Poisson's ratio $\gamma = 0.3$, and density $\rho = 7607$ kg/m^3. It was observed that the elastic modulus obtained in this paper (145 GPa) is lower than that of general steel (~200 GPa), which was also observed in 3D-printed 316L steel of other studies [12,62]. There may be two reasons for this phenomenon. The first is that the elastic modulus is very sensitive to the elastic range selected for calculating it. The second is that the material properties fabricated by the 3D printing technology may be worse than the general material. Besides, the structures in the study experience extensive plastic deformation, and the effect of elastic modulus on structural response is negligible. In conclusion, the stress–strain curve obtained from the uniaxial tensile test is considered reliable and suitable for use in the study.

3.2. Model validation

In this study, the tensile specimens and four types of 316L steel tubes were fabricated using commercial 316 stainless steel powder based on selective laser melting (SLM). The chemical composition of the powder is listed in Table 1 and the fabricated 316 specimens are shown in Fig. 5 (b).

To validate the accuracy of the FE model, the experiment was performed by utilizing the Zwick HB250 testing machine with a speed of 4

Table 1
Chemical composition inspection report of 316 stainless steel powder.

Element	Fe	Cr	Ni	Mo	Mn	Si
wt. %	/	16-18	10-14	2-3	0-2	0-1

mm/min (Fig. 5). Specifically, the geometric parameters of the tested origami pattern tube were $b = 60$ mm, $c = 16.292$ mm, $l = 30$ mm, and $t_1 = t_2 = t_3 = 1$ mm. As shown in Fig. 6, it was observed that the simulated and experimental force–displacement curves for the four origami multi-cell structures generally agreed in terms of fluctuations and average force. However, the initial peak forces of experiment results were observed to be higher than that of simulation results. This may be attributed to manufacturing defects in the specimens. Overall, the finite element model was accurate enough to simulate the origami multi-cell structure and was used for the subsequent numerical analysis and optimization. As shown in Fig. 6(a) and (b), the maximum peak force and average force were adopted by W2W structures, and the lowest peak force was attained by the W2C structure.

As for the deformation mode, four different origami multi-cell tubes were compared in Fig. 6. It was observed that almost every origami module was folded by following the pre-designed diamond origami pattern for W2W and W2C structures and the origami creases deformed to two sides as shown in Fig. 6(a) and (b). However, as depicted in Fig. 6 (c) and (d), C2C and C2W structures did not follow the pre-designed origami pattern, and the origami creases deformed laterally. The deformation mode following the redesigned origami pattern is desirable by sweeping more area and producing more membrane energy, which helps to enhance energy absorption. The reason for this difference is the cross-section characteristic of the four multi-cell structures. Specifically, for W2W and W2C structures, the ribs were connected to the web of the outer origami tubes, which cannot interrupt the deformation of the pre-designed patterns (see Fig. 7). It was observed that the deformation was mainly initiated from the corner (see Fig. 7(a) and (b)). However, for C2C and C2W structures, the ribs are connected to the corner of the outer origami tubes, which is the middle line of origami patterns. The connecting ribs prevented the middle valleys of the origami pattern (red dotted line in Fig. 7(c) and (d)) from moving inward, which were forced to move sideways along with the origami patterns.

As shown in Fig. 6, it was interesting to find that the W2C and C2C structures introduced a progressive layer-by-layer deformation pattern, while the W2W and C2W structures deformed irregularly. Specifically, for the W2W structure (see Fig. 6(a)), the left side of the second origami module and the right side of the third module collapsed first in the experimental results, and then the left side of the first module began to collapse. In the simulation results, the W2W structures collapsed in a layer-by-layer mode from the top. There may be some manufacturing defect randomly distributed in the inner wall and outer wall, which weakened different parts of the structure. When ribs connect to the
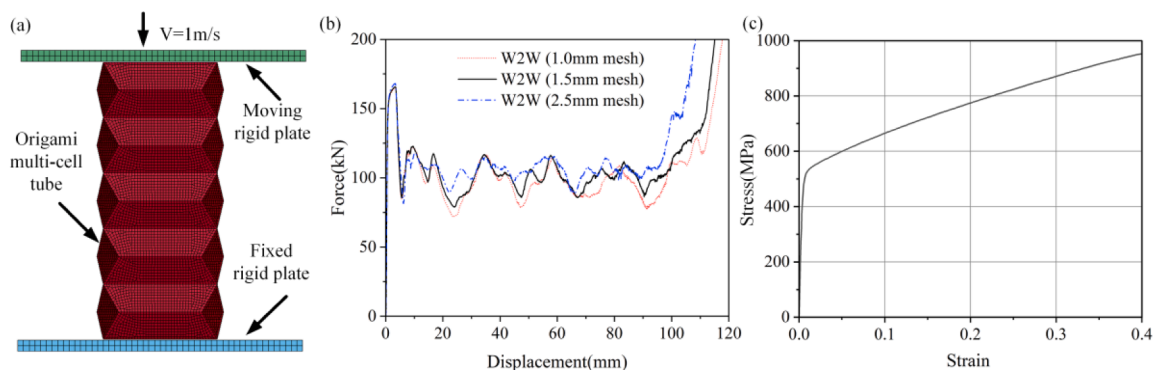

Fig. 4. (a) Numerical model of origami multi-cell structure, (b) convergence study of element size, (c) true stress–strain curve obtained by the uniaxial tensile test of the 316L stainless steel specimen.
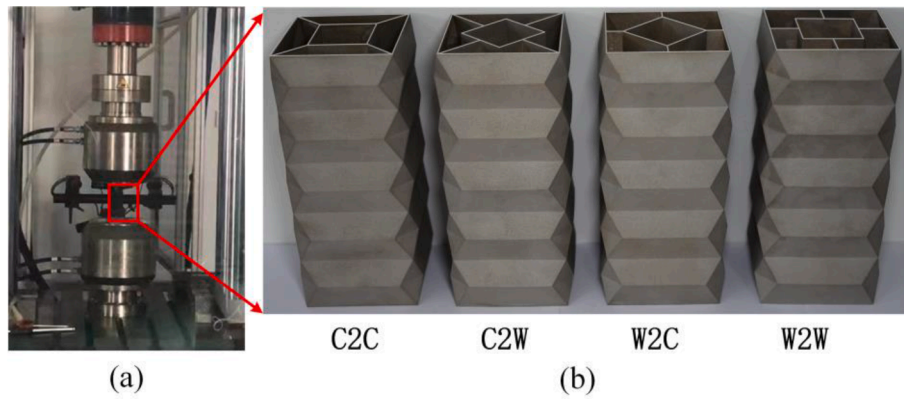
Fig. 5. Installation of the specimen and the as-built 316L specimens of four types of geometrical structures for (a) installation of a specimen, (b) the as-built 316L specimens including C2C, C2W, W2C, and W2W.
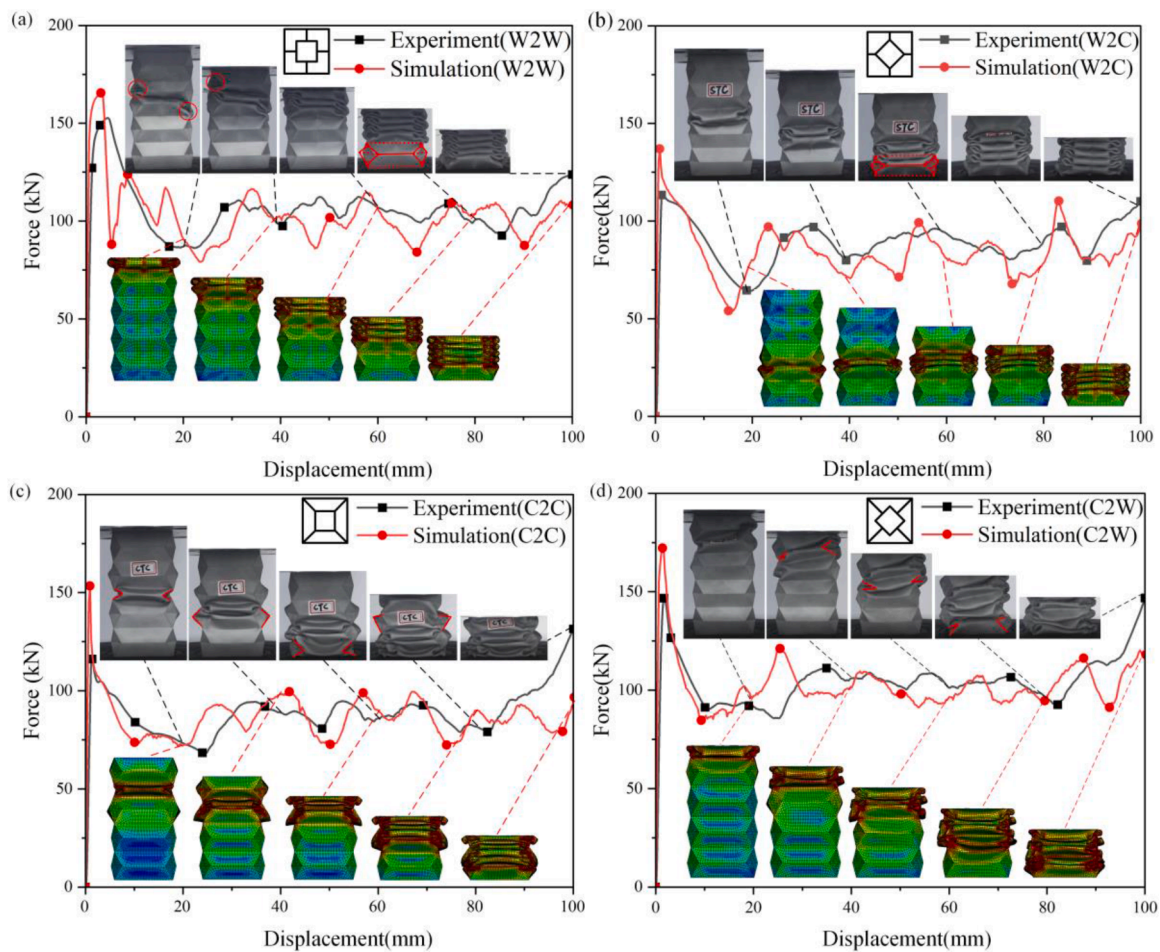

Fig. 6. Comparison of experimental and simulation results based on the force–displacement curves and deformation (The deformation plots for simulation and experimental comparison are reflected at displacement $d = 20, 40, 60, 80, 100$ mm respectively.) (a) W2W, (b) W2C, (c) C2C, (d) C2W.

corner of the inner walls (W2C and C2C), there is a strong interaction between the outer origami tube, the rib plate, and the inner tube, which results in a layer-by-layer deformation mode (see Fig. 6(b) and (c)). Because the deformation of the rectangular tube is initiated by the four corners. However, for W2W and C2W, the web connection between the inner tube and the rib plates results in a more flexible deformation compared to the corner connection. Therefore, the non-progressive and unstable deformation modes occurred for these structures due to the manufacturing defects during the loading process in the experiment (see

Fig. 6(a) and (d)). The results concluded that W2C structures excelled in forming progressive diamond deformation mode.

Overall, the W2W type origami multi-cell structures are most promising for energy absorption and W2C type outcomes for low peak force and excellent deformation mode.
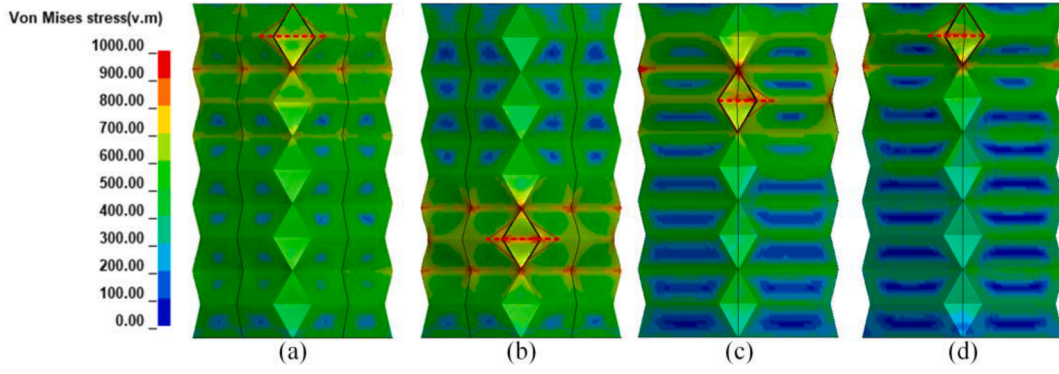
Fig. 7. Von Mises stress contours at the displacement of 4 mm for (a)W2W, (b)W2C, (c)C2C, and (d) C2W.

4. A Bayesian optimization algorithm for multi-objective crashworthiness optimization

This section introduces a novel Bayesian optimization with Gaussian Processes to effectively address the challenge of handling mixed categorical-continuous design variables. Subsequently, the multi-objective optimization problem of origami multi-cell structures is formally defined. The discussion encompasses optimization outcomes, focusing on energy absorption capacity and deformation modes. To underscore the effectiveness of this optimization method, a comparative analysis is conducted against baseline origami multi-cell structures.

4.1. Bayesian optimization algorithm based on Hamming distances

4.1.1. Modeling mixed categorical-continuous variables using the Gaussian process

Gaussian Process (GP) Model has proven to be a flexible and effective surrogate model for expensive non-linear responses. It is especially suited for sparse data (X, Y) or $(x^{(i)}, y^{(i)})$, where $x^{(i)}$ is a vector of n_d-dimensional input at the i_{th} data and $y^{(i)}$ is the associated output, where $i = 1, 2, \ldots, n$. For a typical GP, the output is given a GP prior distribution with zero mean and a covariance kernel. The predictive power of GP is governed by the kernel function. To model the categorical inputs with continuous variables, we use a kernel that combines a categorical kernel based on Hamming distances and the squared-exponential kernel into the form as in Eq. (3) [63].

$$K\left(\left(x^{(i)}, c^{(i)}\right), \left(x^{(j)}, c^{(j)}\right)\right) = K_{cont_1}\left(x^{(i)}, x^{(j)}\right) + K_{cat_1}\left(c^{(i)}, c^{(j)}\right) \\ + K_{cont_2}\left(x^{(i)}, x^{(j)}\right) \times K_{cat_2}\left(c^{(i)}, c^{(j)}\right) \tag{3}$$

where $x^{(i)}$ and $x^{(j)}$ are the continuous variables, $c^{(i)}$ and $c^{(j)}$ are the categorical variables, K_{cont_1} and K_{cont_2} are the squared-exponential kernels with different length scales, K_{cat_1} and K_{cat_2} are the categorical kernels with different length scales. The squared-exponential kernel is adopted as in Eq. (4) [53]:

$$k_{cont}\left(x^{(i)}, x^{(j)}\right) = \frac{1}{\lambda_0} \exp\left\{ -\sum_{r=1}^{n_d} \beta_m \left(x_r^{(i)} - x_r^{(j)}\right)^2 \right\} \tag{4}$$

where r_{th} is the dimension of input, and $1/\lambda_0$ and β_m represent the process variance and the length scale, respectively. The categorical kernel is adopted as in Eq. (5) [53]:

$$k_{cat}\left(c^{(i)}, c^{(j)}\right) = exp\left(-\frac{dist\left(c^{(i)}, c^{(j)}\right)}{\beta_q} \right) \tag{5}$$

where $dist(c^{(i)}, c^{(j)})$ is 1 if $c^{(i)} = c^{(j)}$, otherwise $dist(c^{(i)}, c^{(j)})$ is 0. β_q denotes the length scale. The marginal likelihood of the GP requires inverting the covariance matrix K defined in Eq. (6) [64], where $\delta_{i,j}$ is the identity matrix:

$$K_{i,j} = k\left(\left(x^{(i)}, c^{(i)}\right), \left(x^{(j)}, c^{(j)}\right)\right) + \frac{1}{\lambda_1}\delta_{i,j} \tag{6}$$

The GP parameters to be fit are the variance and noise parameters. The marginal log-likelihood for GP with the given dataset (X, Y) is shown in Eq. (7) [65]. Since the model does not provide gradients for the categorical variables, optimization of the acquisition function was performed in a mixed fashion, i.e., treating the categorical variables as discrete optimization variables.

$$\log P(Y|X) = -\frac{1}{2}Y^T K^{-1} Y - \frac{1}{2}\log|K| - \frac{n}{2}\log(2\pi) \tag{7}$$

The model prediction is a Gaussian distribution with mean $\widehat{y}(x^*)$ in Eq.(8) [65] and variance $\widehat{v}(x^*)$ in Eq.(9) [65], where $k(x^*, x^*)$ is self-covariance for the test point x^*, and $k(x^*, x)$ is the kernel evaluated between the x^* and samples/dataset x:

$$y(x^*) = k((x^*, c^*), (\mathbf{x}, \mathbf{c}))^T K^{-1} Y \tag{8}$$

$$v(x^*) = k((x^*, c^*), (x^*, c^*)) - k((x^*, c^*), (\mathbf{x}, \mathbf{c}))^T K^{-1} k((x^*, c^*), (\mathbf{x}, \mathbf{c})) \tag{9}$$

4.1.2. Bayesian optimization

The primary goal of the Bayesian optimization algorithm (BO) is to establish a probabilistic model that effectively captures the behavior of the black-box objective being optimized. Initially, the objective values associated with each point in the input space are used to establish a prior distribution, typically employing a GP in our study. Once objective values for the input points are acquired, the predictive distribution is subsequently updated, transitioning into the posterior distribution. This updated distribution informs us about the potential objective values for each point in the input space and guides the selection of the most promising locations for enhancing the probabilistic model. The strategy for locating these points is defined by the acquisition function.

For multi-objective optimization, various approaches are available, including Pareto fronts-based methods and weighted sum approaches. We adopt the latter to handle multi-objective optimization. This approach transforms the multi-objective problem into a single-objective one, and for BO, we adopt the Expected Improvement (EI) acquisition function. EI effectively balances exploration and exploitation within the design space by leveraging the uncertainty information provided by the GP. Exploitation involves sampling where the GP predicts a high objective value, while exploration involves sampling at locations where prediction uncertainty is high. Both scenarios result in elevated acquisition function values, and the objective is to maximize the acquisition function to determine the next sampling point.

Fig. 8 illustrates the function of BO, showcasing the black-box function before and after BO in Fig. 8(a) and (b), respectively. By utilizing the acquisition function, we can identify promising points characterized by high prediction uncertainty (shaded area) and improved goal values (dotted line), as depicted in Fig. 8(a). Fig. 8(b) shows the
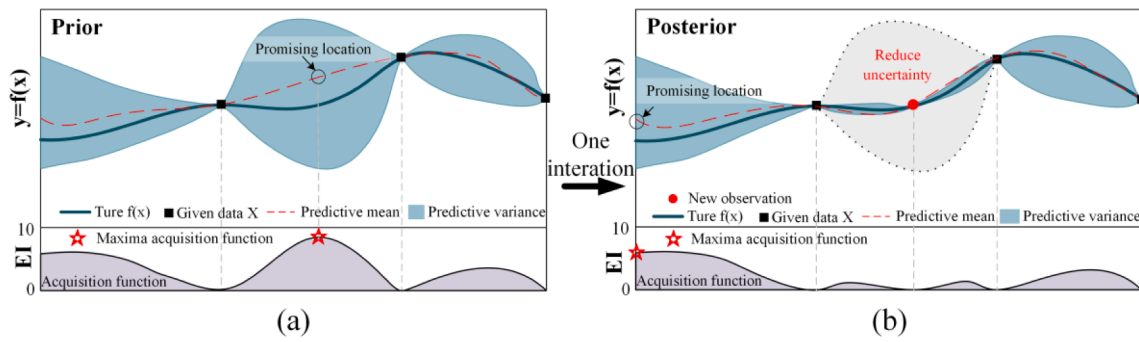
Fig. 8. The function of Bayesian optimization: (a) prior and (b) posterior distributions. The acquisition function identifies promising points, contributing to the enhancement of model quality through increased certainty at these points.

impact of incorporating a new point, leading to a significant reduction in uncertainty in the vicinity of the added point and the assessment of new promising locations. This concludes one iteration of the BO process, effectively achieving both exploration and exploitation objectives concurrently.

EI is defined as in Eq. (10) [66], where $f(\mathbf{x}^+)$ is the value of the best sample so far. The EI can be evaluated analytically under the GP model assuming normal distribution as in Eq. (11) [67].

$$EI(\mathbf{x}) = E max(f(\mathbf{x}) - f(\mathbf{x}^+), 0) \tag{10}$$

$$EI(\mathbf{x}) = (y(\mathbf{x}) - f(\mathbf{x}^+) - \xi)\Phi(Z) + \sigma(\mathbf{x})\phi(Z) \tag{11}$$

where [68]

$$Z = \frac{y(\mathbf{x}) - f(\mathbf{x}^+) - \xi}{\sigma(\mathbf{x})} \tag{12}$$

where $\widehat{\sigma}(\mathbf{x})$ is the standard deviation of the GP posterior prediction. Φ and ϕ are the CDF (cumulative distribution function) and PDF (probability density function) of the standard normal distribution, respectively. The first summation term in Eq. (11) is the exploitation term and the second is the exploration term. Parameter ξ determines the amount of exploration during optimization and higher ξ values lead to more exploration and are set to be 0.01.

To further illustrate the optimization process of the multi-cell tube, the flow chart is shown in Fig. 9. The optimization algorithm is mainly performed in Python, coupled with numerical simulations utilizing LS-DYNA.

4.2. Design of multi-objective optimization problem

The origami pattern design is essential for triggering the collapse mode of the origami multi-cell structures and thus affecting their energy-absorbing characteristics. In this optimization study, five design parameters are analyzed, namely folding angle θ and modulus number M, the thickness of outer wall t_1, thickness of ribs t_2, and thickness of inner wall t_3. In this case, the studied origami parameters M is set from 3 to 12, θ is set from 120° to 170° and the thicknesses of different parts

vary from 0.7 mm to 2.0 mm. Besides, four types of origami multi-cell structures were investigated in this study, i.e., W2W, W2C, C2C, and C2W. For each type of origami multi-cell structure, 10 initial sampling points were selected. Therefore, the initial surrogate models were built based on the 40 initial sampling points, which were distributed in the design space using the Latin hypercube sampling (LHS) method. The sequential sampling strategy was adopted by adding 10 new training points at each optimization iteration, and the optimized result was finally attained after convergence. The target response values of the 120 training sample points were obtained from finite element simulations.

To quantitatively evaluate the energy-absorbing performance of these origami multi-cell structures, two important design criteria were utilized in this study, i.e., specific energy-absorbing capability (*SEA*) and maximum force (F_{max}) [69]. A small F_{max} is preferred because the large maximum force can produce large impact acceleration and even cause severe injuries to the passengers. *SEA* is a key indicator to consider both the energy-absorbing capability and the mass, which can be expressed as:

$$SEA = \frac{EA}{m} = \frac{\int_0^d F(s)\mathrm{d}s}{m} \tag{13}$$

where F denotes the force at the loading distance s and d is the total loading displacement. In this study, d is set as 86 mm. EA is the energy-absorbing capability at the displacement d and m is the total mass of the tube. In a crash, the energy absorber is expected to absorb as much energy as possible, so that less energy is transferred to passengers. On the other hand, lightweight is pursued to save fuel consumption. Thus, a large value of *SEA* indicates excellent energy absorption efficiency.

While assuming the "*SEA*" and "F_{max}" are equally important, the weighted sum approach for the multi-objective optimization was adopted as formulated in Eq. (14), where SEA_{norm} and $F_{maxnorm}$ are the normalized values according to Eqs. (15) and (16), respectively. The minimum and maximum values are estimated from the training dataset and are updated for each optimization cycle.

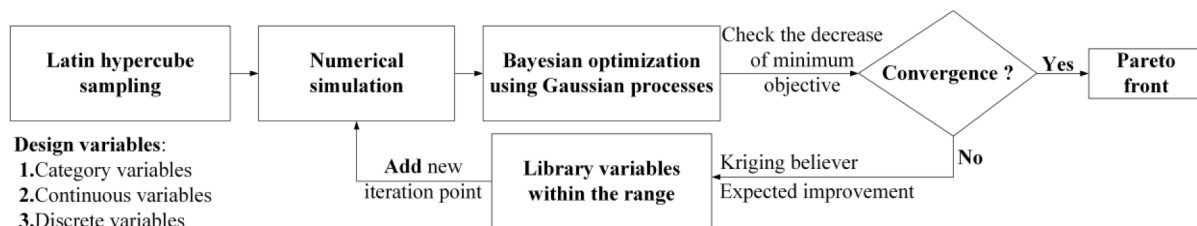$$obj = SEA_{norm} + F_{maxnorm} \tag{14}$$

Fig. 9. The flow chart of Bayesian optimization. The optimization is considered to be converged when the decrease of the minimum objective for two consecutive iterations is less than 1.0×10^{-6}.

$$SEA_{norm} = -\frac{SEA - \min(SEA)}{\max(SEA) - \min(SEA)} \quad (15)$$

$$F_{maxnorm} = \frac{F_{max} - \min(F_{max})}{\max(F_{max}) - \min(F_{max})} \quad (16)$$

Therefore, the multi-objective optimization problem is given as

$$\begin{cases} obj = \min\{-SEA_{norm}(\theta, M, t_1, t_2, t_3, C) + F_{maxnorm}(\theta, M, t_1, t_2, t_3, C)\} \\ s.t.\ 3 \leq M \leq 12\ (M \in N*) \\ 120° \leq \theta \leq 170°\ (\theta \in N*) \\ 0.7\ mm \leq t_1, t_2, t_3 \leq 2.0\ mm \\ Configuration\ categories\ C \in \{C2C,\ C2W,\ W2W,\ W2C\} \end{cases} \quad (17)$$

Where $C \in \{C2C,\ C2W,\ W2W,\ W2C\}$ is the categorical variable. The proposed BO method was utilized to obtain the Pareto optimal solution set and the corresponding Pareto frontier.

4.3. Multi-objective optimization result

The optimization results were obtained after several iterations of progressively adding points, the optimization results were depicted in Fig. 10. The Pareto fronts, as depicted in Fig. 10(a), showed no significant improvements from the 6th iteration to the 8th iteration. Furthermore, no decrease in the minimum objective during the 7th iteration and the 8th iteration, as presented in Fig. 10(b). Therefore, the convergence criteria were satisfied after the 8th iteration. It was also interesting to find that most added points were from W2C for the sequential iterations, which means these origami-multi-cell structures have the potential for better performance among the four origami multi-cell structures. This may be due to the stable and progressive deformation mode of origami W2C structures.

The optimization results show that the two objectives conflict with each other, i.e., the *SEA* decreases as the F_{max} decreases and vice versa. The Pareto frontier provides an insightful understanding of the relationship between the optimization objectives and offers more design options for the energy-absorbing capability structure. To show the convergence process, the Pareto fronts of initial samples, 6th, 7th, and 8th iterations were compared in Fig. 10(a). Compared to the Pareto front of the initial samples, the Pareto front for the 8th iteration moved toward the bottom left corner, demonstrating the effectiveness of the optimization algorithm.

It was observed that the total number of samples was 120 for this mixed categorical-continuous variable design problem. However, for each conventional five-variable optimization problem, typically 50 initial samples (10 times the number of design variables) are needed,

which indicates that at least 200 samples are needed to build accurate surrogate models of acceptable accuracy. For this nonlinear design problem, even more samples may be needed to achieve a desirable accuracy. The results conclude that the proposed Bayesian optimization method can efficiently deal with mixed categorical-continuous variables problems by using at least 66.67 % fewer samples and fully exploring the potential of the promising structures. Considering the fact that the calculation time of each FE model is 3 h and the processing time of the optimization loop is within 1 min with the computer of 8 kernel i5-CP11400F@2.60 GHz CPU and 16GB RAM. Therefore, the proposed optimization method is very promising for complicated and time-consuming problems.

Therefore, the Pareto front of the 8th iteration was considered as the optimization results, and the final optimal design was then obtained based on the minimum distance selection method (TMDSM) [70] (red star point in Fig. 10). To quantitatively evaluate the energy-absorbing performance of the origami multi-cell structure after optimization, the selected optimal solution was compared with the conventional multi-cell W2C and the baseline design.

The multi-cell structure and thickness of conventional W2C structure were set to the same as the optimal W2C. To keep the same mass, the height of the conventional W2C was set to 144.56 mm. The comparison between the optimal and multi-cell W2C was obtained by force-–displacement curves and energy–displacement curves as shown in Fig. 11. Compared with conventional multi-cell W2C, the optimal origami W2C greatly decreased the maximum force F_{max} by 30.69 % with the similar *SEA*. The related results are listed in Table 2.

Moreover, the comparison between the optimal and baseline W2C was obtained by force–displacement curves, energy–displacement curves, and deformation in Fig. 12. The related results are listed in Table 3. It was interesting to find that the *SEA* of the origami multi-cell structure after BO increased by 40 % and the maximum force F_{max} was almost similar. Because the optimum and baseline designs are all origami structures, their peak force already decreased a lot compared with the conventional multi-cell structures and were hard to further improve. As for the deformation mode, the optimal and baseline W2C designs were collapsed in a progressive and uniform deformation mode as shown in Fig. 12, which is pre-designed by their origami structures. In Fig. 12(c) and (d), it was observed that the number of origami modulus in the outer wall of the optimal W2C design increased from 5 to 12 compared to the baseline W2C structures. Therefore, the force-–displacement curve of the optimal design was more stable than that of the baseline design (see Fig. 12(a)). In conclusion, the advantage of the origami multi-cell W2C in energy absorption property was observed.
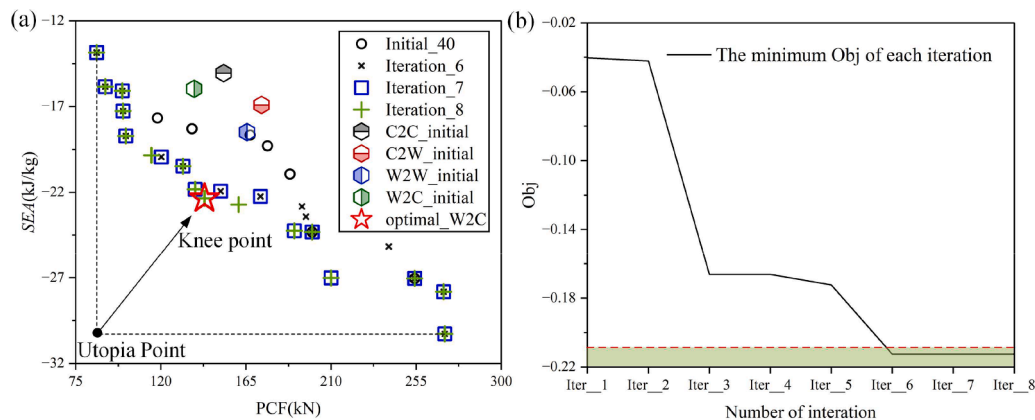

Fig. 10. Pareto fronts of origami multi-cell structures (The red star-shaped point was the optimum design. And it was determined by the minimum distance selection method (TMDSM), which was the closest point to the utopia point.), (b) the minimum objective for different optimization iterations.
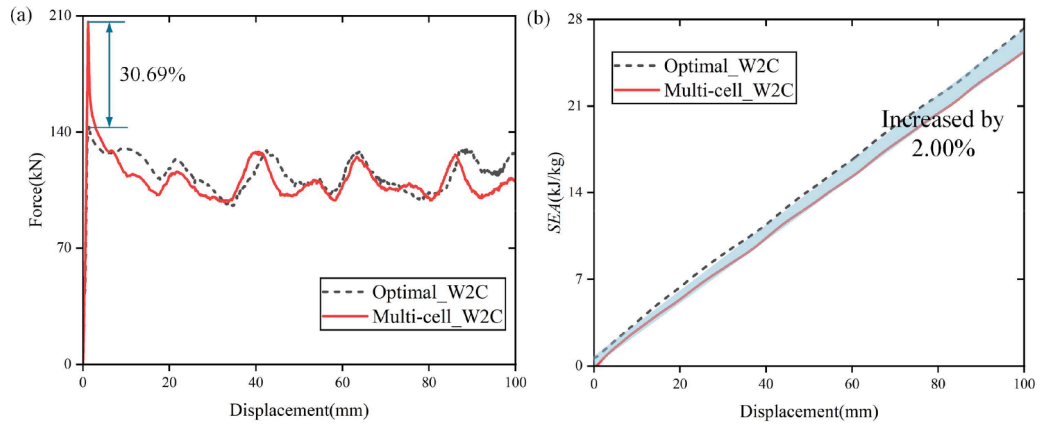
Fig. 11. Comparison optimization results of optimized and conventional multi-cell W2C: (a) force–displacement curves and (b) energy–displacement curves.

Table 2
Comparison of energy-absorbing capability characteristics of the optimized and conventional multi-cell W2C.

Tube	F_{max}(kN)	F_{max} reduction	*SEA* (kJ/kg)	*SEA* increase
Optimal W2C	143.10	30.69 %	22.35	2.00 %
Conventional W2C	206.47	–	21.91	–

5. Conclusions

In this paper, the energy-absorbing capability of four cross-sectional types of origami multi-cell structures with different folding angles, modulus numbers, and thicknesses was studied. To optimize the design parameters of four origami multi-cell structures, the Bayesian optimization method based on Hamming distance was utilized to handle the mixed categorical-continuous variable problem. The main conclusions are summarized as follows:

(1) Among the four origami multi-cell tubes in our study cases, the web-to-web (W2W) type origami multi-cell structures are most promising for energy absorption and web-to-corner (W2C) type outcomes for low peak force and good deformation mode. The results concluded that the web connection of the rib and outer wall facilitates the formation of diamond deformation mode and the corner connection of the rib and inner wall helps to deform in a stable and progressive mode.

(2) A novel Bayesian optimization algorithm based on Hamming distance was proposed to handle the mixed categorical-continuous variable problem. Specifically, the origami multi-cell optimization problem includes continuous variables (three wall thickness), discrete variables (origami folding angle and modulus number), and categorical variables (four types of

Table 3
Comparison of energy-absorbing capability characteristics of the optimized and baseline W2C.

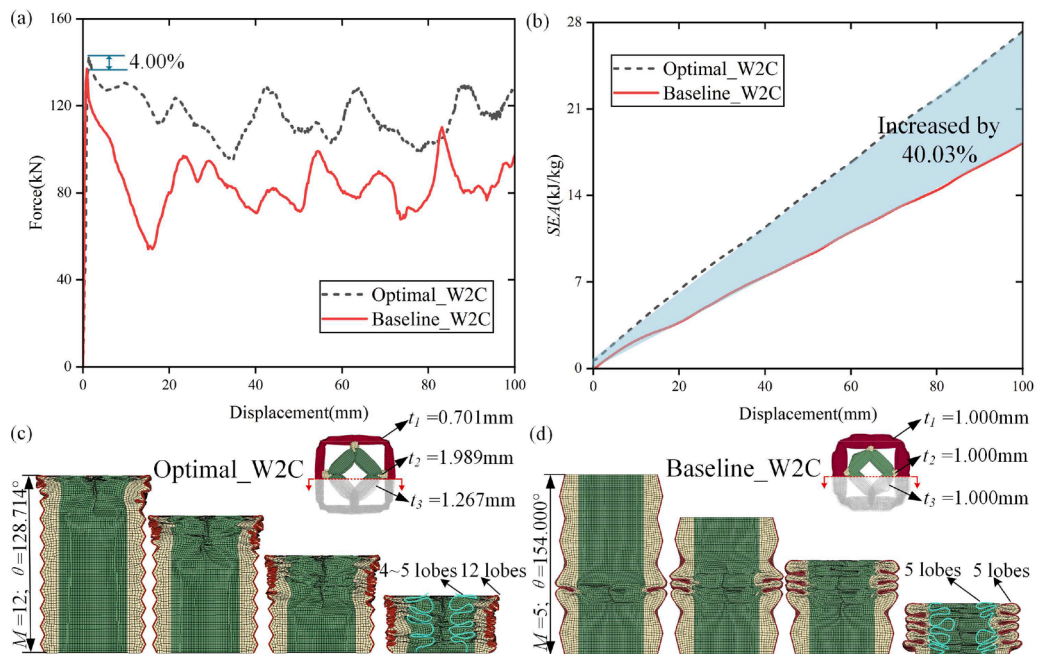| Tube	F_{max}(kN)	F_{max} reduction	*SEA* (kJ/kg)	*SEA* increase
Optimal W2C	143.10	−4.00 %	22.35	40.03 %
Baseline W2C	137.59	–	15.96	–

Fig. 12. Comparison optimization results of optimized and baseline W2C: (a) force–displacement curves, (b) energy–displacement curves, (c) cross-sectional view of baseline W2C, (d) cross-sectional view of optimized origami multi-cell structure.

origami multi-cell structures). The results indicated that the proposed Bayesian optimization method can efficiently explore the design space of the promising structures and save at least 66.67 % computational cost.

(3) The obtained optimal W2C origami multi-cell structure exhibited excellent energy-absorbing capability performance. Compared with the conventional multi-cell W2C, the maximum force F_{max} of optimal W2C origami multi-cell structure was decreased by 30 % while keeping a similar *SEA*. Compared with the baseline origami multi-cell W2C, the energy-absorbing capability of optimal W2C origami multi-cell was improved by 40 % with a similar maximum force F_{max}.

In this study, the uncertainty of design variables, the discrepancy between experimental and model predictions, different weights for the different objectives, and the dynamic performance of the origami multi-cell structure were not considered and will be studied in our future research. Besides, the discrete variable type might be more appropriate for the thickness variable if the manufacturing process is taken into account, especially for some manufacturing methods with low precision, which can also be considered in the future study.

CRediT authorship contribution statement

Na Qiu: Writing – review & editing, Writing – original draft, Supervision, Conceptualization. **Zhuoqun Yu:** Data curation. **Depei Wang:** Visualization, Validation. **Mingwei Xiao:** Software, Investigation, Formal analysis. **Yiming Zhang:** Writing – review & editing, Writing – original draft, Supervision, Software, Methodology. **Nam H. Kim:** Writing – review & editing, Supervision. **Jianguang Fang:** Writing – review & editing, Supervision, Conceptualization.

Declaration of competing interest

The authors declare that they have no known competing financial interests or personal relationships that could have appeared to influence the work reported in this paper.

Data availability

Data will be made available on request.

Acknowledgments

References

[1] Q. Wang, S. Li, Z. Liu, G. Wu, J. Lei, Z. Wang, Geometric design and energy absorption of a new deployable cylinder tube, Mech. Adv. Mater. Struct. 29 (2022) 1911–1924, https://doi.org/10.1080/15376494.2020.1846099.
[2] S. Pirmohammad, S.E. Marzdashti, Crashworthiness optimization of combined straight-tapered tubes using genetic algorithm and neural networks, Thin-Walled Struct. 127 (2018) 318–332, https://doi.org/10.1016/j.tws.2018.01.022.
[3] A. Baykasoğlu, C. Baykasoğlu, E. Cetin, Multi-objective crashworthiness optimization of lattice structure filled thin-walled tubes, Thin-Walled Struct. 149 (2020) 106630, https://doi.org/10.1016/j.tws.2020.106630.
[4] X. An, Y. Gao, J. Fang, G. Sun, Q. Li, Crashworthiness design for foam-filled thin-walled structures with functionally lateral graded thickness sheets, Thin-Walled Struct. 91 (2015) 63–71, https://doi.org/10.1016/j.tws.2015.01.011.
[5] Y. Li, Z. Fan, S. Hu, F. Zhang, L. Hu, Z. Xue, Dynamic enhancement mechanism of energy absorption of multi-cell thin-walled tube, Thin-Walled Struct. 178 (2022) 109449, https://doi.org/10.1016/j.tws.2022.109449.
[6] X. Deng, W. Liu, Experimental and numerical investigation of a novel sandwich sinusoidal lateral corrugated tubular structure under axial compression, Int. J. Mech. Sci. 151 (2019) 274–287, https://doi.org/10.1016/j.ijmecsci.2018.11.010.
[7] H. Sun, C. Ge, Q. Gao, N. Qiu, L. Wang, Crashworthiness of sandwich cylinder filled with double-arrowed auxetic structures under axial impact loading, Int. J. Crashworthiness 27 (2022) 1383–1392, https://doi.org/10.1080/13588265.2021.1947071.
[8] N. Qiu, Y. Gao, J. Fang, G. Sun, N.H. Kim, Topological design of multi-cell hexagonal tubes under axial and lateral loading cases using a modified particle swarm algorithm, Appl. Math. Model. 53 (2018) 567–583, https://doi.org/10.1016/j.apm.2017.08.017.
[9] H. Zeng, W. Shi, H. Lv, N. Qiu, C. Ma, Q. Gao, Crashworthiness analysis and optimization of a novel "cake-cutting" multi-cell tube, Thin-Walled Struct. 192 (2023) 111160, https://doi.org/10.1016/j.tws.2023.111160.
[10] N. Qiu, C. Park, Y. Gao, J. Fang, G. Sun, N.H. Kim, Sensitivity-based parameter calibration and model validation under model error, J. Mech. Des. 140 (2018) 011403, https://doi.org/10.1115/1.4038298.
[11] N. Qiu, J. Zhang, F. Yuan, Z. Jin, Y. Zhang, J. Fang, Mechanical performance of triply periodic minimal surface structures with a novel hybrid gradient fabricated by selective laser melting, Eng. Struct. 263 (2022) 114377, https://doi.org/10.1016/j.engstruct.2022.114377.
[12] N. Qiu, Y. Wan, Y. Shen, J. Fang, Experimental and numerical studies on mechanical properties of TPMS structures, Int. J. Mech. Sci. (2023) 108657, https://doi.org/10.1016/j.ijmecsci.2023.108657.
[13] H. Yin, W. Zhang, L. Zhu, F. Meng, J. Liu, G. Wen, Review on lattice structures for energy absorption properties, Compos. Struct. 304 (2023) 116397, https://doi.org/10.1016/j.compstruct.2022.116397.
[14] F. Wu, Y. Chen, S. Zhao, Y. Hong, Z. Zhang, S. Zheng, Mechanical properties and energy absorption of composite bio-inspired multi-cell tubes, Thin-Walled Struct. 184 (2023) 110451, https://doi.org/10.1016/j.tws.2022.110451.
[15] N.S. Ha, T.M. Pham, H. Hao, G. Lu, Energy absorption characteristics of bio-inspired hierarchical multi-cell square tubes under axial crushing, Int. J. Mech. Sci. 201 (2021) 106464, https://doi.org/10.1016/j.ijmecsci.2021.106464.
[16] A. Najafi, M. Rais-Rohani, Mechanics of axial plastic collapse in multi-cell, multi-corner crush tubes, Thin-Walled Struct. 49 (2011) 1–12, https://doi.org/10.1016/j.tws.2010.07.002.
[17] H. Zhang, D. Yu, D. Wang, T. Li, Y. Peng, L. Hou, Z. Li, Crashworthiness of nested corrugation square energy-absorbing tubes with circumferentially cosine profile, Mech. Adv. Mater. Struct. 0 (2023) 1–18, https://doi.org/10.1080/15376494.2023.2257694.
[18] Q. Gao, L. Wang, Y. Wang, C. Wang, Multi-objective optimization of a tapered elliptical tube under oblique impact loading, Proc. Inst. Mech. Eng., Part D: J. Automobile Eng. 231 (2017) 1978–1988, https://doi.org/10.1177/0954407017690963.
[19] D.H. Chen, S. Ozaki, Numerical study of axially crushed cylindrical tubes with corrugated surface, Thin-Walled Struct. 47 (2009) 1387–1396, https://doi.org/10.1016/j.tws.2008.12.008.
[20] S. Wu, G. Li, G. Sun, X. Wu, Q. Li, Crashworthiness analysis and optimization of sinusoidal corrugation tube, Thin-Walled Struct. 105 (2016) 121–134, https://doi.org/10.1016/j.tws.2016.03.029.
[21] S.E. Alkhatib, M.S. Matar, F. Tarlochan, O. Laban, A.S. Mohamed, N. Alqwasmi, Deformation modes and crashworthiness energy absorption of sinusoidally corrugated tubes manufactured by direct metal laser sintering, Eng. Struct. 201 (2019) 109838, https://doi.org/10.1016/j.engstruct.2019.109838.
[22] N.S. Ha, G. Lu, Thin-walled corrugated structures: a review of crashworthiness designs and energy absorption characteristics, Thin-Walled Struct. 157 (2020) 106995, https://doi.org/10.1016/j.tws.2020.106995.
[23] X.M. Xiang, G. Lu, Z. You, Energy absorption of origami inspired structures and materials, Thin-Walled Struct. 157 (2020) 107130, https://doi.org/10.1016/j.tws.2020.107130.
[24] K. Yang, S. Xu, J. Shen, S. Zhou, Y.M. Xie, Energy absorption of thin-walled tubes with pre-folded origami patterns: numerical simulation and experimental verification, Thin-Walled Struct. 103 (2016) 33–44, https://doi.org/10.1016/j.tws.2016.02.007.
[25] K. Yang, S. Xu, S. Zhou, Y.M. Xie, Multi-objective optimization of multi-cell tubes with origami patterns for energy absorption, Thin-Walled Struct. 123 (2018) 100–113, https://doi.org/10.1016/j.tws.2017.11.005.
[26] X. Zhang, G. Lu, S. Wang, Y. Durandet, Mechanical characteristics of graded origami bellows under axial tension, Front. Phys. 11 (2023) 1304426, https://doi.org/10.3389/fphy.2023.1304426.
[27] S. Liu, W. Lv, Y. Chen, G. Lu, Deployable prismatic structures with rigid origami patterns, J. Mech. Robot. 8 (2016) 031002, https://doi.org/10.1115/1.4031953.
[28] L. De Waal, G. Lu, J. Zhang, Z. You, Dynamic behaviour of graded origami honeycomb, Int. J. Impact Eng. 157 (2021) 103976, https://doi.org/10.1016/j.ijimpeng.2021.103976.
[29] A.G. Mamalis, D.E. Manolakos, G.L. Viegelahn, N.M. Vaxevanidis, W. Johnson, The inextensional collapse of grooved thin-walled cylinders of PVC under axial loading, Int. J. Impact Eng. 4 (1986) 41–56, https://doi.org/10.1016/0734-743X(86)90026-6.
[30] S.J. Hosseinipour, G.H. Daneshi, Energy absorbtion and mean crushing load of thin-walled grooved tubes under axial compression, Thin-Walled Struct. 41 (2003) 31–46, https://doi.org/10.1016/S0263-8231(02)00099-X.
[31] G.H. Daneshi, S.J. Hosseinipour, Grooves effect on crashworthiness characteristics of thin-walled tubes under axial compression, Mater. Des. 23 (2002) 611–617, https://doi.org/10.1016/S0261-3069(02)00052-3.
[32] A. Alavi Nia, R. Rahpeima, S. Chahardoli, I. Nateghi, Evaluation of the effect of inner and outer transverse and longitudinal grooves on energy absorption characteristics of cylindrical thin-walled tubes under quasi-static axial load, Int. J.

Crashworthiness 24 (2019) 1–12, https://doi.org/10.1080/13588265.2017.1367356.

[33] M. j. Rezvani, M. Damghani Nouri, H. Rahmani, Experimental and numerical investigation of grooves shape on the energy absorption of 6061-T6 aluminium tubes under axial compression, Int. J. Mater. Struct. Integr. 6 (2012) 151–168, https://doi.org/10.1504/IJMSI.2012.049953.

[34] J. Song, Y. Chen, G. Lu, Axial crushing of thin-walled structures with origami patterns, Thin-Walled Struct. 54 (2012) 65–71, https://doi.org/10.1016/j.tws.2012.02.007.

[35] C. Zhou, Y. Zhou, B. Wang, Crashworthiness design for trapezoid origami crash boxes, Thin-Walled Struct. 117 (2017) 257–267, https://doi.org/10.1016/j.tws.2017.03.022.

[36] J. Ma, H. Dai, M. Shi, L. Yuan, Y. Chen, Z. You, Quasi-static axial crushing of hexagonal origami crash boxes as energy absorption devices, Mech. Sci. 10 (2019) 133–143, https://doi.org/10.5194/ms-10-133-2019.

[37] C. Zhou, B. Wang, J. Ma, Z. You, Dynamic axial crushing of origami crash boxes, Int. J. Mech. Sci. 118 (2016) 1–12, https://doi.org/10.1016/j.ijmecsci.2016.09.001.

[38] L.M. Fonseca, G.V. Rodrigues, M.A. Savi, An overview of the mechanical description of origami-inspired systems and structures, Int. J. Mech. Sci. 223 (2022) 107316, https://doi.org/10.1016/j.ijmecsci.2022.107316.

[39] J. Ma, S. Chai, Y. Chen, Geometric design, deformation mode, and energy absorption of patterned thin-walled structures, Mech. Mater. 168 (2022) 104269, https://doi.org/10.1016/j.mechmat.2022.104269.

[40] R. Yao, T. Pang, B. Zhang, J. Fang, Q. Li, G. Sun, On the crashworthiness of thin-walled multi-cell structures and materials: state of the art and prospects, Thin-Walled Struct. 189 (2023) 110734, https://doi.org/10.1016/j.tws.2023.110734.

[41] C.H. Zhou, B. Wang, H.Z. Luo, Y.W. Chen, Q.H. Zeng, S.Y. Zhu, Quasi-static axial compression of origami crash boxes, Int. J. Appl. Mech. 09 (2017) 1750066, https://doi.org/10.1142/S1758825117500661.

[42] M. Abolfathi, A.A. Nia, Optimization of energy absorption properties of thin-walled tubes with combined deformation of folding and circumferential expansion under axial load, Thin-Walled Struct. 130 (2018) 57–70, https://doi.org/10.1016/j.tws.2018.05.011.

[43] L. Hou, H. Zhang, Y. Peng, S. Wang, S. Yao, Z. Li, G. Deng, An integrated multi-objective optimization method with application to train crashworthiness design, Struct. Multidiscip. Optim. 63 (2021) 1513–1532, https://doi.org/10.1007/s00158-020-02758-2.

[44] K.-H. Lee, J.-W. Yi, J.-S. Park, G.-J. Park, An optimization algorithm using orthogonal arrays in discrete design space for structures, Finite Elem. Anal. Des. 40 (2003) 121–135, https://doi.org/10.1016/S0168-874X(03)00095-7.

[45] G. Sun, H. Yu, Z. Wang, Z. Xiao, Q. Li, Energy absorption mechanics and design optimization of CFRP/aluminium hybrid structures for transverse loading, Int. J. Mech. Sci. 150 (2019) 767–783, https://doi.org/10.1016/j.ijmecsci.2018.10.043.

[46] J.S. Arora, M.W. Huang, C.C. Hsieh, Methods for optimization of nonlinear problems with discrete variables: a review, Struct. Optim. 8 (1994) 69–85, https://doi.org/10.1007/BF01743302.

[47] J. Fang, N. Qiu, X. An, F. Xiong, G. Sun, Q. Li, Crashworthiness design of a steel–aluminum hybrid rail using multi-response objective-oriented sequential optimization, Adv. Eng. Softw. 112 (2017) 192–199, https://doi.org/10.1016/j.advengsoft.2017.05.013.

[48] Y. Peng, T. Li, C. Bao, J. Zhang, G. Xie, H. Zhang, Performance analysis and multi-objective optimization of bionic dendritic furcal energy-absorbing structures for trains, Int. J. Mech. Sci. 246 (2023) 108145, https://doi.org/10.1016/j.ijmecsci.2023.108145.

[49] N. Qiu, Y. Gao, J. Fang, Z. Feng, G. Sun, Q. Li, Theoretical prediction and optimization of multi-cell hexagonal tubes under axial crashing, Thin-Walled Struct. 102 (2016) 111–121, https://doi.org/10.1016/j.tws.2016.01.023.

[50] Z. Li, W. Ma, S. Yao, P. Xu, L. Hou, G. Deng, A machine learning based optimization method towards removing undesired deformation of energy-absorbing structures, Struct. Multidiscip. Optim. 64 (2021) 919–934, https://doi.org/10.1007/s00158-021-02896-1.

[51] R. Gómez-Bombarelli, J.N. Wei, D. Duvenaud, J.M. Hernández-Lobato, B. Sánchez-Lengeling, D. Sheberla, J. Aguilera-Iparraguirre, T.D. Hirzel, R.P. Adams, A. Aspuru-Guzik, Automatic chemical design using a data-driven continuous representation of molecules, ACS Cent. Sci. 4 (2018) 268–276, https://doi.org/10.1021/acscentsci.7b00572.

[52] R. Jenatton, C. Archambeau, J. González, M. Seeger, Bayesian optimization with tree-structured dependencies, in: Proceedings of the 34th International Conference on Machine Learning, PMLR, 2017, pp. 1655–1664, in: https://proceedings.mlr.press/v70/jenatton17a.html (accessed August 27, 2023).

[53] F. Hutter, Automated Configuration of Algorithms For Solving Hard Computational Problems, University of British Columbia, 2009, https://doi.org/10.14288/1.0051652.

[54] F. Hutter, Automated configuration of algorithms for solving hard computational problems, (n.d.). https://doi.org/10.14288/1.0051652.

[55] M. Halstrup, Black-box optimization of mixed discrete-continuous optimization problems, (2016). https://doi.org/10.17877/DE290R-17800.

[56] E.C. Garrido-Merchán, D. Hernández-Lobato, Dealing with categorical and integer-valued variables in Bayesian optimization with Gaussian processes, Neurocomputing 380 (2020) 20–35, https://doi.org/10.1016/j.neucom.2019.11.004.

[57] S. Solorio-Fernández, J.A. Carrasco-Ochoa, J.F. Martínez-Trinidad, A survey on feature selection methods for mixed data, Artif. Intell. Rev. 55 (2022) 2821–2846, https://doi.org/10.1007/s10462-021-10072-6.

[58] S. Pirmohammad, S.E. Marzdashti, Crushing behavior of new designed multi-cell members subjected to axial and oblique quasi-static loads, Thin-Walled Struct. 108 (2016) 291–304, https://doi.org/10.1016/j.tws.2016.08.023.

[59] J. Ma, Z. You, Energy absorption of thin-walled square tubes with a prefolded origami pattern—part i: geometry and numerical simulation, J. Appl. Mech. 81 (2014) 011003, https://doi.org/10.1115/1.4024405.

[60] N.S. Ha, G. Lu, X. Xiang, High energy absorption efficiency of thin-walled conical corrugation tubes mimicking coconut tree configuration, Int. J. Mech. Sci. 148 (2018) 409–421, https://doi.org/10.1016/j.ijmecsci.2018.08.041.

[61] X.W. Zhang, H. Su, T.X. Yu, Energy absorption of an axially crushed square tube with a buckling initiator, Int. J. Impact Eng. 36 (2009) 402–417, https://doi.org/10.1016/j.ijimpeng.2008.02.002.

[62] C. Li, J. Fang, Y. Wan, N. Qiu, G. Steven, Q. Li, Phase field fracture model for additively manufactured metallic materials, Int. J. Mech. Sci. 251 (2023) 108324, https://doi.org/10.1016/j.ijmecsci.2023.108324.

[63] H. Luo, Y. Cho, J.W. Demmel, X.S. Li, Y. Liu, Hybrid models for mixed variables in Bayesian optimization, (2022). http://arxiv.org/abs/2206.01409 (accessed June 15, 2023).

[64] C. Bishop, Pattern recognition and machine learning, Springer Google Scholar 2 (2006) 531–537.

[65] J. Luo, Z. Fu, Y. Zhang, W. Fu, J. Chen, Aerodynamic optimization of a transonic fan rotor by blade sweeping using adaptive Gaussian process, Aerosp. Sci. Technol. 137 (2023) 108255, https://doi.org/10.1016/j.ast.2023.108255.

[66] X. Wang, Y. Jin, S. Schmitt, M. Olhofer, Recent advances in Bayesian optimization, (2022). http://arxiv.org/abs/2206.03301 (accessed August 27, 2023).

[67] D.R. Jones, M. Schonlau, W.J. Welch, Efficient global optimization of expensive black-box functions, J. Glob. Optim. 13 (1998) 455–492, https://doi.org/10.1023/A:1008306431147.

[68] Y. Zhang, S. Ghosh, T. Vandeputte, L. Wang, Bayesian Optimization for Multi-Objective High-Dimensional Turbine Aero Design, American Society of Mechanical Engineers Digital Collection, 2021, https://doi.org/10.1115/GT2021-59745.

[69] Q. Gao, X. Zhao, C. Wang, L. Wang, Z. Ma, Multi-objective crashworthiness optimization for an auxetic cylindrical structure under axial impact loading, Mater. Des. 143 (2018) 120–130, https://doi.org/10.1016/j.matdes.2018.01.063.

[70] F. Xiong, D. Wang, S. Chen, Q. Gao, S. Tian, Multi-objective lightweight and crashworthiness optimization for the side structure of an automobile body, Struct. Multidiscip. Optim. 58 (2018) 1823–1843, https://doi.org/10.1007/s00158-018-1986-3.